

# Pulsed 1.5- $\mu\text{m}$ LIDAR for Axial Aircraft Wake Vortex Detection Based on High-Brightness Large-Core Fiber Amplifier

Agnès Dolfi-Bouteyre, Guillaume Canat, Matthieu Valla, Béatrice Augère, Claudine Besson, Didier Goular, Laurent Lombard, Jean-Pierre Cariou, Anne Durecu, Didier Fleury, Laurent Bricteux, Sebastien Brousmiche, *Member, IEEE*, Sébastien Lukan, *Member, IEEE*, and Benoit Macq, *Fellow, IEEE*

**Abstract**—In this paper, we present the development of an axial aircraft wake vortex light detection and ranging (LIDAR) sensor, working in Mie scattering regime, based on pulsed 1.5- $\mu\text{m}$  high-brightness large-core fiber amplifier. An end-to-end Doppler heterodyne LIDAR simulator is used for the LIDAR design. The simulation includes the observation geometry, the wake vortex velocity image, the scanning pattern, the LIDAR instrument, the wind turbulence outside the vortex, and the signal processing. An innovative high-brightness pulsed 1.5- $\mu\text{m}$  laser source is described, based on a master oscillator power fiber amplifier (MOPFA) architecture with a large-core fiber. The obtained beam quality is excellent ( $M^2 = 1.3$ ), and achieved pulsed energy is 120  $\mu\text{J}$  with a pulse repetition frequency of 12 kHz and a pulse duration of 800 ns. A Doppler heterodyne LIDAR is developed based on this laser source with a high-isolation free-space circulator. The LIDAR includes a real-time display of the wind field. Wind dispersion is postprocessed. Field tests carried out at Orly airport in April 2008 are reported. Axial aircraft wake vortex signatures have been successfully observed and acquired at a range of 1.2 km with axial resolution of 75 m for the first time with fiber laser source.

**Index Terms**—Heterodyne light detection and ranging (LIDAR), large-core fiber, LIDAR, pulsed fiber amplifier, wake vortex.

## I. INTRODUCTION

**D**ETECTING atmospheric hazards such as wake vortices, wind shear, and clear air turbulence has been a major concern for 20 years. In order to increase the operation capacity of the air transport system, it is of interest to minimize the separation between aircrafts during takeoff and landing. Previous

Manuscript received October 1, 2008; revised November 19, 2008 and November 20, 2008. First published February 2, 2009; current version published April 8, 2009. This work was supported by the European Union under Grant 12008 (FIDELIO program).

A. Dolfi-Bouteyre, G. Canat, M. Valla, B. Augère, C. Besson, D. Goular, L. Lombard, A. Durecu, and D. Fleury are with the French Aeronautics and Space Research Center (ONERA), the French Aerospace Laboratory, Palaiseau 91761, France (e-mail: agnes.dolfi-bouteyre@onera.fr; guillaume.canat@onera.fr; matthieu.valla@onera.fr; beatrice.augere@onera.fr; claudine.besson@onera.fr; didier.goular@onera.fr; laurent.lombard@onera.fr; anne.durecu@onera.fr).

J.-P. Cariou was with the French Aeronautics and Space Research Center (ONERA), the French Aerospace Laboratory, Palaiseau 91761, France. He is now with Leosphere Company, Orsay 91400, France (e-mail: jpcariou@leosphere.fr).

L. Bricteux, S. Brousmiche, S. Lukan, and B. Macq are with the Université Catholique de Louvain (UCL), 1348 Louvain-la-Neuve, Belgium (e-mail: laurent.bricteux@uclouvain.be; brousmiche@tele.ucl.ac.be; lukan@tele.ucl.ac.be; benoit.macq@uclouvain.be).

Color versions of one or more of the figures in this paper are available online at <http://ieeexplore.ieee.org>.

Digital Object Identifier 10.1109/JSTQE.2008.2010463

developments have already demonstrated that coherent detection light detection and rangings (LIDARs) offer a practical and efficient tool to monitor and characterize wind fields, and, more specifically, wake vortices [1], [2].

LIDAR systems used to date are based on solid-state laser technologies that do not meet commercial aircraft requirements for onboard implementation due to high power consumption, size, weight, reliability, and life cycle cost. It was therefore the purpose of FIDELIO European project to introduce a unique fiber laser technology geared for the aerospace industry requirements, enabling onboard realization of an atmospheric hazard detection LIDAR system.

The basis of FIDELIO LIDAR is the remote measurement of windtracer velocities using coherent detection and fiber architecture based on mainstream telecommunication components. FIDELIO LIDAR's goal is to detect wake vortices along their axis at range of 2 km.

The electrical to optical efficiency of 1.5- $\mu\text{m}$  fiber laser sources is of the order of 10%, thus allowing low electrical consumption. This wavelength is also the most favorable for eye-safe LIDAR designs: the eye-safety laser energy limitation being high, the laser power can be increased with little constraints on the LIDAR operation or design. One advantage of the IR fiber technology is its reliability. It is now well established that a fiber architecture is easy to adjust and mechanically reliable in a vibrating environment. Recently, 1.5- $\mu\text{m}$  fiber coherent LIDARs have been successfully flown [3]. The other advantages of fiber architectures are their compacity and flexibility in terms of onboard installation. The LIDAR can be split up into subsystems spatially far apart in the aircraft body and linked together using fiber optics. The new technology of large-mode-area (LMA) fibers enable high peak power generation without nonlinear effects.

Air particles producing Mie scattering play the role of windtracers. The LIDAR measures the wind velocity component projected on its line of sight (LOS) using the Doppler shift. A pulsed laser allows to spatially resolve the wind field along its LOS and scanning of the laser enables to generate an accurate 3-D velocity image of the wind field. In-flight demonstration has been made during IWAKE UE program [4].

FIDELIO project activities encompass the fiber laser design, the LIDAR simulations and design, and the field tests on Orly airport.

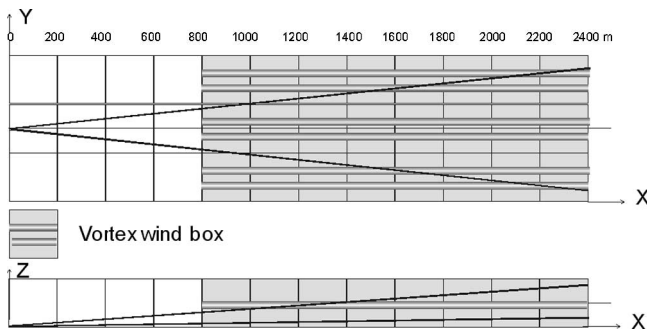


Fig. 1. Modeling wind field construction with UCL wind boxes.

Section II describes the end-to-end simulation tool developed for laser and LIDAR architecture specifications. The results obtained on the laser source development are presented in Section III. The choices in LIDAR architecture are discussed in Section IV. Field test results are given in Section V.

## II. LIDAR MODELING

In order to specify the adequate laser, the French Aeronautics and Space Research Center (ONERA) has developed an end-to-end simulation tool. The simulations take into account the observation geometry, the wake vortex velocity image, the scanning pattern, the LIDAR instrument, the wind turbulence outside the vortex, and the signal processing. A simulation of large aircraft wake vortex evolution in a turbulent atmosphere has been performed by the Université Catholique de Louvain (UCL)/TERM.

The geometry for the simulated wind field construction is presented in Fig. 1. Three wind boxes, each including one wake vortex pair, are used in order to show the influence of the angle of view. Because of higher radial velocities (projection of the 3-D air velocity on the LIDAR laser axis), lateral vortices are easier to detect than in line vortices. The scan pattern is sinusoidal with horizontal and vertical fields of view of  $12^\circ$  and  $3^\circ$ , respectively. The frame rate is 0.2 Hz. The angle of view of the scanner is pointed toward the  $3^\circ$  glideslope.

The radial velocity for a 20-s-old wake vortex pair (young vortices) located 1600 m away from the LIDAR is presented in Fig. 2. The velocity values are coded in color. For this example of the scanning pattern centered on the wake vortex pair, radial velocity varies from  $-1.3$  to  $0.9$  m/s. The sinusoidal scan pattern is superimposed.

### A. Modeling Assumptions

First, the simulator builds the wind field around the scan pattern by paving the whole area with individual cubic wind fields provided by UCL, with either turbulence-only or vortex distribution. It then computes the projection of the global 3-D wind field on each LIDAR LOS corresponding to each laser pulse by 2-D interpolation on the velocity grid. LOS orientation is computed from the LIDAR position and scanning pattern. Computation is operated for range gates having a length of 200 m. Data are then concatenated and sorted by pulse number.

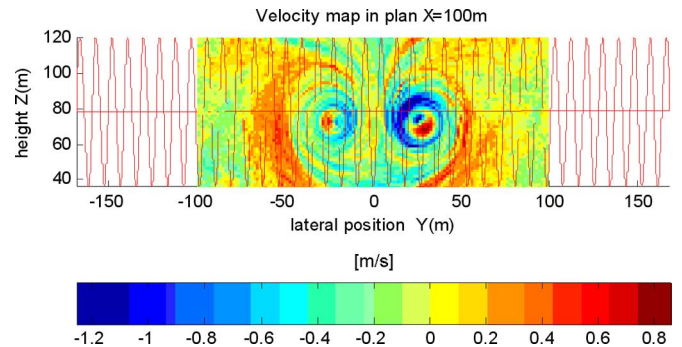


Fig. 2. Radial velocity of wake vortex model (UCL/TERM) + scanning pattern.

The simulator second step computes the temporal LIDAR signal for each emitted pulse from the radial velocity on every point of the LOS, the atmospheric parameters, and LIDAR parameters.

The simulator third step processes the time series, analyzing the spectral content in each range gate. Pulses are averaged into angular pixels. The signal processing is based on a Fourier transform maximum likelihood estimator (see Appendix for more details). The outputs are mean velocity, velocity dispersion, and carrier to noise ratio (CNR) for each range gate and each angular pixel.

Then the code compares the ideal image we could process from the wind dispersion with the one observed by the LIDAR. The results are sorted using the computed quality score.

The LIDAR model is based on a “feuilleté” [5] model. It includes effects of laser beam propagation in the instrument and the atmosphere, diffraction, defocus, refractive turbulence, Mie scattering on aerosols, laser speckle, and receiver noise [6]. The laser beam shape (which is a critical aspect of large-core fiber amplifier) is introduced by its  $M^2$  beam quality factor affecting the Gaussian beam divergence.

### B. Modeling Results

To estimate the LIDAR performance, we compute a correlation coefficient  $CC$  between the LIDAR measured dispersion image [Fig. 3(a)] and the theoretical dispersion image [Fig. 3(b)]. This coefficient  $CC$  is the normalized covariance of the two images (LIDAR simulation dispersion image and theoretical dispersion image) calculated at zero.

When  $CC = 1$ , images are perfectly proportional to one another. Even for a value of  $CC = 0.9$ , images are quite similar. This score is never zero except for special cases (orthogonal images). We can consider that a score of  $CC = 0.3$  corresponds to independent images without correlation.

For vortex pattern detection, the correlation score threshold (CCT) has to be adjusted, depending on the detection algorithm and the number of frames considered. For the LIDAR design, CCT was set to 0.7.

Example of the simulation outputs is shown in Fig. 4: the correlation coefficient  $CC$  is drawn as a function of range for various pulse durations and two vortex ages. The LIDAR energy is  $E = 1$  mJ and its pulse rate frequency (PRF) is 4 kHz. For

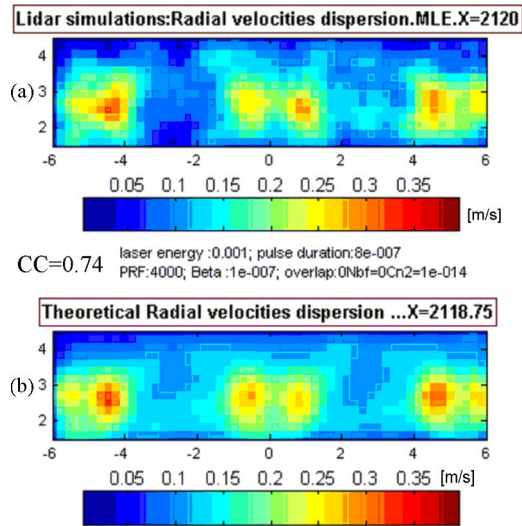


Fig. 3. LIDAR simulation images using the following parameters: pulse energy  $E = 1$  mJ; pulse duration of 800 ns; pulse repetition frequency of 4 kHz; atmospheric backscattering coefficient  $\beta = 1 \times 10^{-7} \text{ m}^{-1} \cdot \text{sr}^{-1}$ ; atmospheric turbulence  $Cn2 = 1 \times 10^{-14} \text{ m}^{-2/3}$ ; range gate of 2120 m. The value of the correlation coefficient for this image is  $CC = 0.74$ .

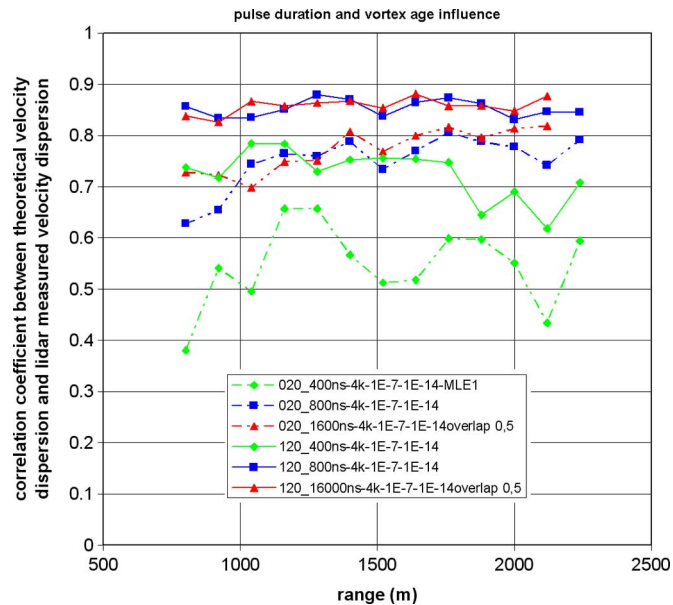


Fig. 4. Correlation coefficient between theoretical velocity dispersion and LIDAR measured velocity dispersion for standard atmosphere (scattering coefficient  $\beta = 1 \times 10^{-7} \text{ m}^{-1} \cdot \text{sr}^{-1}$  and  $Cn2 = 1 \times 10^{-14} \text{ m}^{-2/3}$ ) and different LIDAR configurations (dashed line: 20-s-old vortex; plain line: 120-s-old vortex; green line for 400 ns pulse duration; blue line for 800 ns pulse duration; red line for 1600 ns pulse duration).

pulse duration 1600 ns, an overlap between consecutive gates of 0.5 is taken for the range gates in order to keep the range resolution. It can be seen that the detection is ensured with 800 and 1600 ns pulse duration ( $CC > 0.7$ ). For shorter pulse (400 ns), the detection of young vortex is not possible because of laser spectral broadening.

The pulse duration must be at least 800 ns. A 1600 ns pulse gives very good simulation results, but was not chosen for the

LIDAR design because such large range gates (240 m) would lead to a system sensitive to wind gradient.

Extensive simulations were carried out with the following parameters varying: laser energy  $E$ , pulse duration PRF, and turbulence factor. The main conclusions are as follows.

- 1) At medium range ( $> 1$  km), the vortex is easier to detect by measuring the spectrum broadening. These results confirm the IWAKE conclusions [4].
- 2) Longer pulse durations (800 ns) give better results than the nominal value of 400 ns and lead to a high-velocity resolution.
- 3) The vortex is easier to detect at later times than at earlier times since dissipation increases the velocity dispersion on the observation axis.
- 4) Low PRF cannot be compensated for by increasing the laser energy. Indeed, a high PRF value enables incoherent summation, reducing speckle effect, and therefore gives a better velocity resolution.
- 5) For PRF = 4 kHz,  $E = 1$  mJ, and for nominal atmospheric conditions, the theoretical LIDAR range is 2400 m. For PRF = 10 kHz,  $E = 0.1$  mJ, and the theoretical LIDAR range is 1200 m.

### III. LASER DEVELOPMENT

Laser source for aerospace application requirements includes, among others, high level of coherence and high energy. In the recent years, the 1  $\mu\text{m}$  fiber lasers have scaled tremendously in energy and power: a few millijoules have been produced in a nonsingle frequency Yb source [7]. For eye-safe 1.5- $\mu\text{m}$  laser sources, erbium-doped fibers have limited absorption and are thus restricted to average power up to about 1 W. Due to the high absorption of Yb ions, erbium-ytterbium double-cladding fibers (DCFs) have enabled amplifier power scaling. These fibers also incorporate a large amount of phosphorous to improve Yb to Er transfer efficiency. However, the phosphorous codoping strongly increases the core refractive index.

When the signal linewidth is very narrow, such as for a coherent detection system, the achievable peak power in fiber amplifiers is limited by stimulated Brillouin scattering (SBS) [8]. Indeed, SBS must be avoided since it reflects the amplified signal toward the local oscillator and can damage optical components. To avoid SBS, the so-called SBS threshold must be increased by shortening the fiber length, reducing the laser intensity, or broadening the laser spectrum (pulse length  $< 10$  ns). In our case, the resolution specifications of the LIDAR lead to pulse duration of several hundreds of nanoseconds that cannot be decreased. The peak power is thus SBS-limited, but SBS threshold can be increased by using LMA fibers [9] that reduce the laser intensity. These fibers must also have low core numerical aperture (NA) to avoid multimode operation detrimental to beam quality for LIDAR efficiency and minimize amplified spontaneous emission (ASE) generation. However, due to phosphorous, the erbium-ytterbium fibers have NAs ranging between 0.11 and to about 0.17. The maximum core diameter for single-mode operation is therefore limited to about 11  $\mu\text{m}$ . A meaningful figure of merit

TABLE I  
PERFORMANCE OF NARROW-LINEWIDTH ERBIUM–YTTERBIUM SOURCES  
COMPATIBLE WITH COHERENT LIDAR APPLICATIONS

$\lambda$ (nm)	Energy (mJ)	$P_{\text{Peak}}$ (W)	$M^2$	PRF (kHz)	Team	R	Year
1536	0.29	2900	2.4	4	ORC [11]	-	2004
1535	1	11000	~5	1	ORC [12]	2.4	2004
1545	0.22	250	1.3	4	ONERA [13]	10	2006
1550	0.053	350	1.1	55	NASA / Acculight [14]	11	2007
1545	0.8	800	1.3	5	ONERA/ IPHT [15]	42	2008

for coherent wind LIDAR range performance is the ratio

$$R = \frac{E\sqrt{\text{PRF}}}{1 + (M^2)^2} \quad (1)$$

where  $E$  is the pulse energy, PRF the pulse repetition rate frequency, and  $M^2$  the beam quality factor. The square of the LIDAR range scales roughly with  $R$ . The larger the  $R$ , the larger the LIDAR performance. Besides high energy and good beam quality, a stable and polarized beam output and long pulses are required. Table I summarizes the performance of erbium–ytterbium master oscillator power fiber amplifier (MOPFA) with our LIDAR application in view. It can be seen that good beam quality and high energy are difficult to achieve.

More elaborate fiber structures have been introduced to reduce the effective core NA [10]. The pedestal structure uses an additional undoped layer around the core. The raised refractive index of this layer reduces the core effective NA, and therefore, the number of modes overlapping to the core. Fig. 5 shows the modeling of the 25- $\mu\text{m}$ -core fiber used in the last stage of our laser. The doped region NA is close to 0.17. However, the surrounding Ge pedestal reduces the effective NA to 0.09. It reduces the number of modes effectively guided into the core to 4 (black solid lines). The high-order modes have a strong overlap with the pedestal and can be filtered by bending.

We have built a MOPFA using a distributed feedback (DFB) laser diode with a linewidth of 600 kHz as oscillator (Fig. 6). The 800 ns pulses are generated by a 1545-nm DFB laser diode associated with an acoustooptic modulator. The first stage amplifier is made of a commercial pure erbium polarization maintaining (PM) fiber. The second stage is composed of a standard single-mode PM erbium–ytterbium fiber. Interstage ASE filtering is required to avoid saturation by the forward propagating ASE. We have thus introduced a 1-nm-wide bandpass filter between each stage and an optical isolator. After the second stage, the pulse energy is 27  $\mu\text{J}$  per pulse at 4 kHz repetition frequency. The last preamplifier stage is made of a 25- $\mu\text{m}$ -core-diameter commercial LMA fiber with 0.1 core NA surrounded by a pedestal similar to the fiber used for modeling in Fig. 5. The cladding diameter is 300  $\mu\text{m}$ . The cladding pump absorption at 975 nm is 3.4 dB/m. This pump wavelength has been chosen to mini-

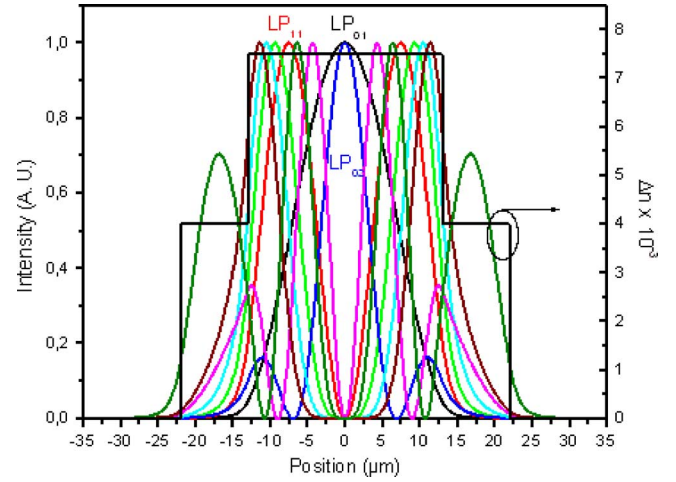


Fig. 5. Modes of the pedestal fiber. The fundamental mode LP01 (black line) and the LP11 mode (red line) are well confined into the core whereas the higher order modes extends deeply into the pedestal.

mize the fiber length and maximize the Brillouin threshold. The pulse energy out of the last stage of the all-fiber MOPFA is 220  $\mu\text{J}$  (Fig. 9). For this measurement, we took into account the interpulse ASE fraction and the average power.

Despite the pedestal fiber structure, four mode groups are still guided by the fiber core. The imperfect mode matching and splice condition at the fiber input lead to higher order modes excitation. Let us assume that a single-mode fiber with amplitude distribution  $\Psi_0$  is spliced to an LMA fiber guiding  $N$  modes with amplitude distribution  $\Psi_k$  and propagation constant  $\beta_k$ . The imperfect splice condition will affect  $\psi_0$  in phase and amplitude, for instance, due to offset between fiber cores, mode adaptation, and/or tilt. The injected field is then  $\psi_{\text{inj}}$ .

The amplitude in the propagating modes (ignoring the nonguided modes) is given by

$$\psi = \sum_{k=0}^N \langle \psi_{\text{inj}}, \psi_k \rangle \psi_k \quad (2)$$

where  $\langle \psi_{\text{inj}}, \psi_k \rangle$  is the scalar product.

After propagation over a fiber length  $L$ , the field is expressed as

$$\psi = \sum_{k=0}^N \langle \psi_{\text{inj}}, \psi_k \rangle \psi_k e^{j\beta_k L} = e^{j\beta_0 L} \sum_{k=0}^N \langle \psi_{\text{inj}}, \psi_k \rangle \psi_k e^{j(\beta_k - \beta_0)L}. \quad (3)$$

Due to temperature and strain fluctuations, the fiber cladding refractive index  $n$  will have small fluctuations  $\delta n$  in real experiments. The mode propagation constants are thus changed by a small deviation proportional to  $\delta n$ . Equation (4) shows that the resulting field will fluctuate accordingly

$$\psi = e^{j\beta_0 L} \sum_{k=0}^N \langle \psi_{\text{inj}}, \psi_k \rangle \psi_k e^{j(\beta_k - \beta_0)L} e^{j(\beta_k - \beta_0)(\delta n/n)L}. \quad (4)$$

Fig. 7 shows the fluctuation of the beam centroid and  $M^2$  (along the  $X$ -direction), assuming the existence of a phase tilt

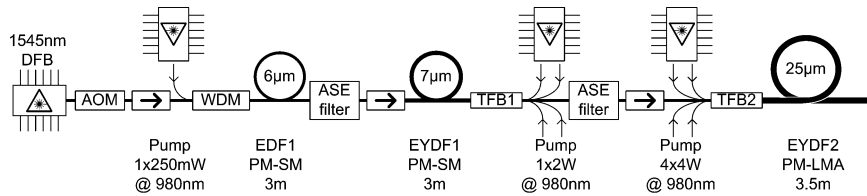


Fig. 6. Setup of the MOPFA laser source. DFB: 600 kHz linewidth laser diode at 1545 nm; AOM: acoustooptical modulator; WDM: pump/signal multiplexer; EDF1: erbium-doped fiber; EYDF1 and EYDF2: erbium–ytterbium codoped fibers; TFB1 and TFB2: tapered fiber bundles.

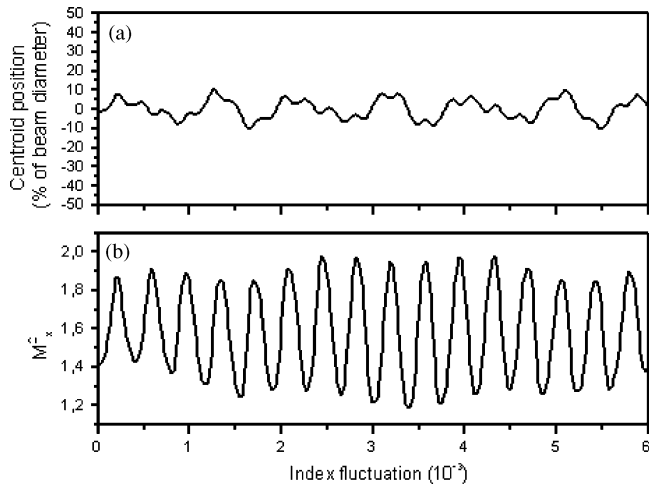


Fig. 7. Centroid position (along the  $X$ -axis) and  $M^2$  evaluated along the  $X$ -axis for the field emerging from the pedestal fiber.

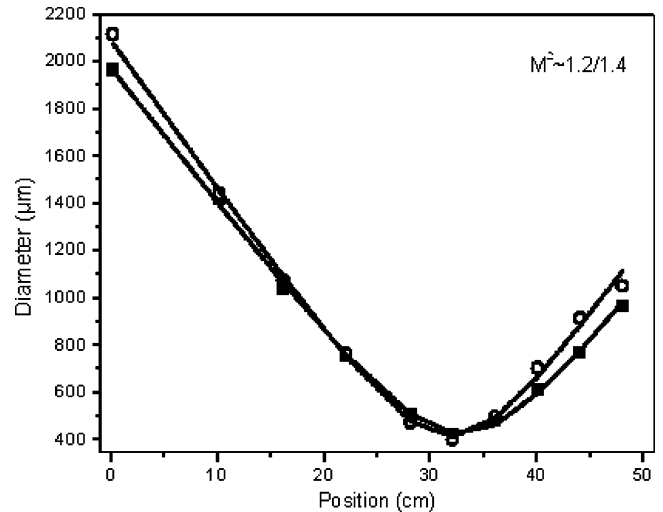


Fig. 8.  $M^2$  measurement along  $X$ - (open symbols) and  $Y$ -axes (full symbols) of the output beam.

of  $1^\circ$  and imperfect mode matching (reflecting the situation at the time of laser build) with injection-mode field diameter of  $14 \mu\text{m}$ . The centroid position and  $M^2$  have been evaluated for the  $X$ -axis using [16]. The interference between the modes generates modulation of these quantities. This can be detrimental to coherent LIDAR operation generating pointing errors and degradation of the heterodyne efficiency. The index modulation period in Fig. 7 is about  $3 \times 10^{-4}$ . The fiber temperature must be controlled within less than 5 K range if we assume that the thermal refractive index change of silica is  $10^{-5} \text{K}^{-1}$ . In our system, special care was taken for the fiber packaging, thus greatly reducing the differential phase fluctuations. The resulting beam quality fluctuates when the laser is switched ON, but quickly stabilizes in a reproducible manner to  $M^2 \sim 1.3$  (Fig. 8). The beam is linearly polarized with a degree of linear polarization better than 98%. In the LIDAR system, the MOPFA was operated at 12 kHz pulse repetition frequency, reaching a pulse energy of  $120 \mu\text{J}$ . The packaging of the MOPFA including the additional pump protections reduced the signal power by 15% attributed to a reduction of the launched pump power.

The high PRF allows hundreds of LIDAR signals to be averaged on each LOS, and thus significantly reduces the speckle noise.

To further improve the laser energy, we have performed preliminary tests using this three-stage amplifier to inject a fourth stage. This last amplifier has been built using a special fiber developed by the Institute of Photonic Technology (IPHT), Jena.

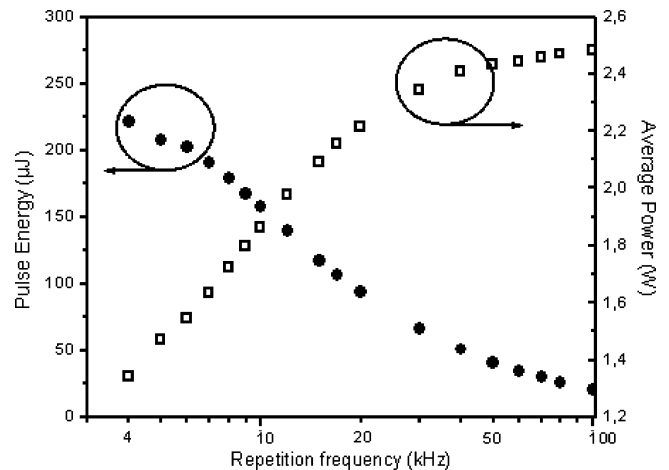


Fig. 9. Output energy (solid symbols) and average power (open symbols) of the laser source before packaging.

The active core is composed of doped erbium–ytterbium filaments and the fiber is single-mode with a core size of about  $30 \mu\text{m}$ . This fiber allowed to extract  $750 \mu\text{J}$  for  $1 \mu\text{s}$  pulses at a repetition rate of 5 kHz. These laboratory results were achieved with a beam quality  $M^2 = 1.3$  [15]. This last prototype has not been integrated for the field test.

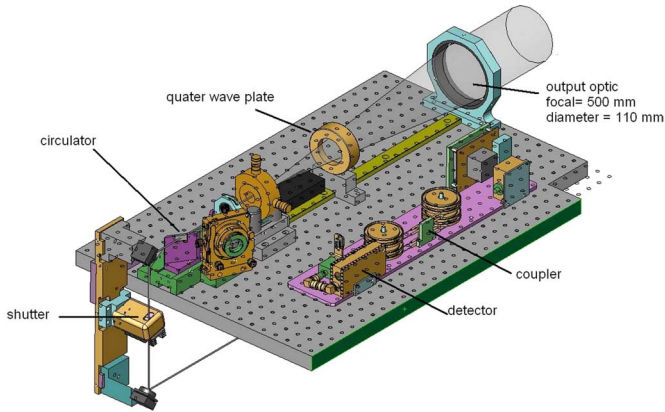


Fig. 10. LIDAR optical layout.

#### IV. LIDAR ARCHITECTURE

##### A. Optical Architecture

The optical architecture was designed with collimated beams, and so, is compatible with different fiber lasers since the laser output is collimated to free space. Fig. 10 shows the LIDAR optical layout. The outgoing and backscattered laser beams are split by polarization selectivity due to the association of a Brewster plate with a quarter-wave plate: this compact laser beam circulation has been specially designed for both robustness and very good optical isolation (60 dB).

The collimated laser beam is emitted horizontally polarized, and thus, is fully transmitted by the Brewster plate. After a pass through a quarter-wave plate and an afocal system, the laser beam is circularly polarized and has an effective Gaussian diameter of 60 mm (at  $1/e^2$ , with  $M^2 = 1.3$ ), allowing a focus range up to 1000 m. The light backscattered by windtracers is collected by the same afocal system. After a second pass through the quarter-wave plate, the backscattered light has vertical polarization and is reflected by the Brewster plate toward a collimator. The backscattered light is focused on a single-mode PM fiber before being mixed with the fibered local oscillator.

In order to retrieve the sign of the Doppler shift, the laser beam frequency is shifted by an acousto-optic modulator before being injected in the amplifier. In our experiment, the value of the frequency shift is 70 MHz.

Fig. 11 is a photograph of LIDAR integration into the “Be-mol” mobile laboratory.

The optimized set of parameters that have been finally integrated for the test campaign was  $E = 120 \mu\text{J}$ , PRF = 12 kHz, and  $M^2 = 1.3$ . Based on the simulation, detection up to 1200 m was then theoretically possible.

##### B. Acquisition and Processing Systems

The synchronization between the LIDAR and the acquisition system is performed by combining the signal used for the laser pulse generation and the trigger signal from the scanner controller. As a delay exists between the pulse generation and its actual emission, a hardware acquisition delay has to be defined. It is estimated by measuring the elapsed time between the

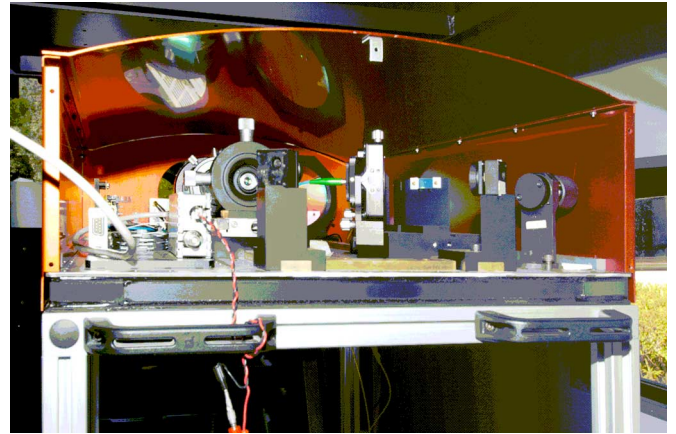


Fig. 11. View of the LIDAR head from the rear. The laser is located under the LIDAR head.

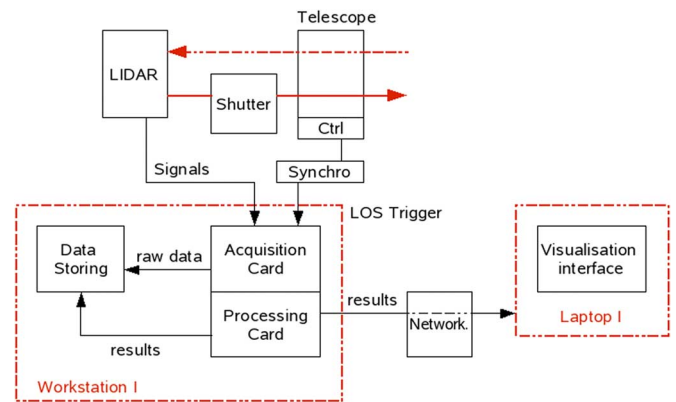


Fig. 12. Acquisition, processing, and visualization system.

trigger edge and the maximum of the laser echo coming from the output lens. The precision range depends on this estimation since it gives the “zero” position. Signals are acquired together with their angular positions for further parameters reconstruction. The scanning pattern shows a good stability of the vertical scanning initial phase. It enables to use the reference scanning profile (implemented in the scanner controller) for the real-time processing. The synchronization board also controls the laser shutter in order to stop the beam as soon as a scanner failure is detected.

Up to 4096, 8-bit samples per signal are acquired at a 500 MHz sampling rate, giving us a range dynamic of about 1200 m. The minimum range can be adjusted by adding an extra acquisition delay. It is typically set to correspond to the end of the blind region. This blind region is determined by the end of the echo signal of the optical emitter lenses. Fig. 12 shows the different parts of the synchronization system.

For each aircraft, a few tens of scans are recorded. The acquisition is started when the aircraft is detected using the video tracking system. The acquired signals are transferred to the processing board through a buffer of multiple redundant array of independent disks (RAID). The results are sent to the main program at the end of each scan during the flyback of the scanner.

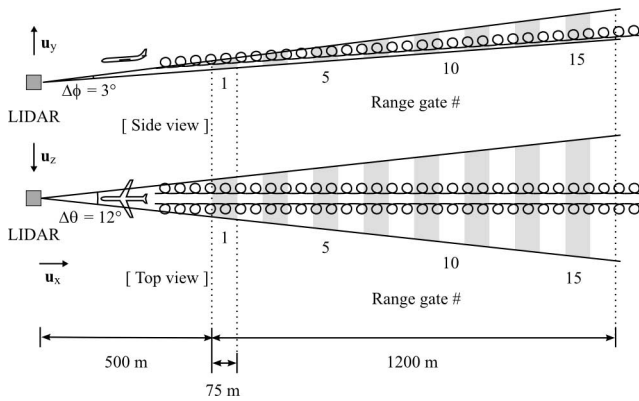


Fig. 13. Scanning configuration.

As shown in Fig. 12, results are sent over a local network to be visualized by one or several independent workstations.

Estimations of mean wind velocity and dispersion are performed on a set of signal samples corresponding to the range gates (Fig. 13). The number of these segments depends on the desired axial resolution. For a given range gate, a wind field image is generated by averaging all the segments spectra corresponding to the same circular region of interest (ROI). In order to increase the SNR, ROI radius is usually chosen higher than the image pixel size. Consequently, a signal segment usually contributes to several neighboring pixels, thus increasing the algorithm computing time.

The information obtained for each range gate image is updated every scan. Up to 16 images are computed per scan corresponding to 16 range gates of 75 m (in the nonoverlapping case). The image resolution has been fixed to  $128 \times 32$  pixels, giving an angular resolution of 1.6 mrad (total field of view is  $12^\circ \times 3^\circ$ ).

Moreover, due to the fact that the aggregation process can be viewed as the projection of a sinusoidal scanning pattern onto a uniform grid, the aggregation level can vary a lot from one pixel to another. It can be seen that in this configuration, the pixels having the higher aggregation level are on the range gate image boundaries, which is not interesting in our case. To reduce this effect on the algorithm execution time, the correspondence table between LOS and pixels is computed at an early stage of the algorithm. By doing this, it becomes possible to equalize the aggregation level over the image by fixing it to a given value  $N$  for all pixels, for instance. In this case, the LOSs for each pixel are sorted depending on the distance to the pixel center in order to select the  $N$  nearest ones. The correspondence table is then inverted in order to be able to assign the LOSs to pixels as they are acquired (in real-time conditions).

The number of signals per scan is determined by the PRF and the scanning period (5 s). Increasing the pulse repetition frequency allows us to decrease the estimation variance of the computed spectra, but does not necessarily improve the image resolution given the fixed sinusoidal scanning pattern.

The average spectra are first processed to isolate the main spectral peak corresponding to the heterodyne signal. In its simplest form, the one implemented in real time, the algorithm



Fig. 14. Aircraft tracking video for distance computations for the wind data (refer to Fig. 15).

only extracts the central peak position (mean velocity), the peak width (velocity dispersion), and its maximum (related to the local SNR).

During postprocessing, the wind velocity dispersion is computed by fitting the logarithm of the spectral peak upper part with a second-order polynomial function. The higher polynomial coefficient is inversely proportional to the peak variance.

## V. FIELD TESTS RESULTS

Field tests were conducted at Orly airport in April 2008. The LIDAR position was about 800 m before the runway touched down threshold, facing landing aircrafts.

The global average wind velocity displayed in the main window has been validated with the atmospheric information coming from the tower.

In order to validate the vortex detection, video recordings of the landing aircraft have been made during the test campaign. A real-time aircraft detection, tracking, and geometric reconstruction algorithm was used in order to track the distance between the aircraft and the sensor (Fig. 14). Moreover, markers have been written on the images whenever a strong-level return signal was received back from the LIDAR, corresponding to a reflection of the beam on the aircraft. This allows validating the results obtained by processing the LIDAR return signal.

Fig. 15 shows a set of wind velocity dispersion images computed after the passing of two successive aircrafts. Each box represents the  $3^\circ \times 12^\circ$  field-of-view image acquired at different ranges (vertical axis) and different times (horizontal axis). We can clearly see the vortex signatures in scans 0 and 1 for the first plane, and in scans 4 and 5 for the second one. The elapsed time between two scans is 6 s. The disappearing of turbulence is mainly due to the lateral wind, moving them outside the spatial region of scan. The distance of the vortex signature corresponds to the distance between the aircraft and the sensor measured by the video detection and tracking system (Fig. 14).

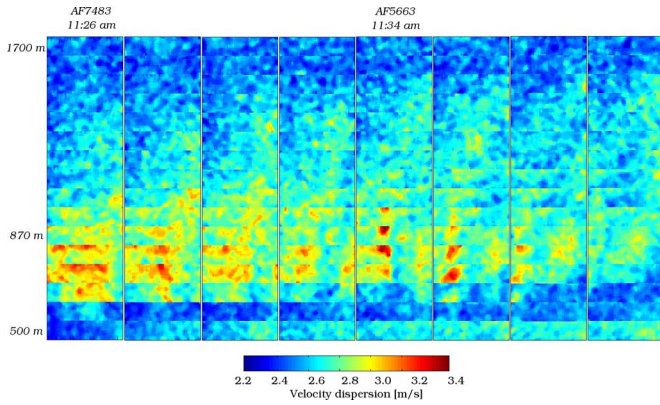


Fig. 15. Velocity dispersion images obtained for eight successive scans of 16 range gates of 75 m.

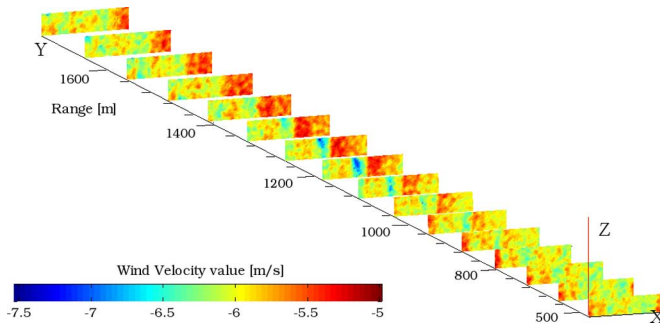


Fig. 16. 3-D view of mean velocity images obtained during landing of a B747 ( $X$ -axis: azimuth scan;  $Y$ -axis: 16 range gates;  $Z$ -axis: elevation scan; color chart: wind velocity).

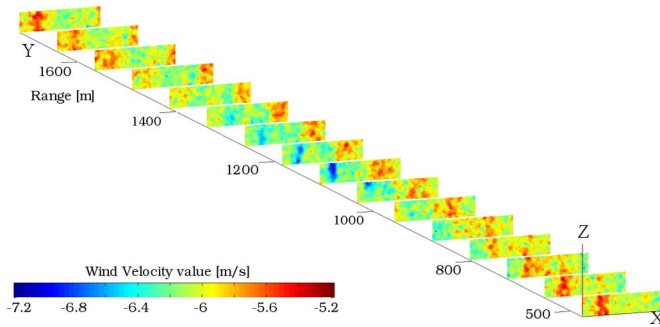


Fig. 17. 3-D view of mean velocity images obtained during landing of a B747 ( $X$ -axis: azimuth scan;  $Y$ -axis: 16 range gates;  $Z$ -axis: elevation scan; color chart: wind velocity).

Figs. 16 and 17 show a 3-D representation of wake vortex detection on two consecutive scans, a few seconds after a B747 landing. Each rectangle corresponds to a range gate. The  $X$ -axis represents the  $12^\circ$  horizontal field of view,  $Z$ -axis the  $3^\circ$  vertical field of view, and  $Y$ -axis the distance of the range gates. The detection was possible on wind velocity that shows strong discontinuities. The blue regions (gates 7–10 around 1.2 km) are again consistent with the aircraft location. We can see the wake vortex decay on the two consecutive scans. This range detection is in accordance with simulated results.

## VI. CONCLUSION

We have presented the development of an axial aircraft wake vortex LIDAR sensor and the field tests results.

An end-to-end Doppler heterodyne LIDAR simulator enabled early performance prediction for LIDAR design. The simulations take into account the observation geometry, the wake vortex velocity image, the scanning pattern, the LIDAR instrument, the wind turbulence outside the vortex, and the signal processing.

An innovative high-brightness pulsed  $1.5\text{-}\mu\text{m}$  laser source has been built based on a MOPFA architecture with a large-core fiber. The beam quality is excellent ( $M^2 = 1.3$ ). Achieved pulsed energy is  $120\ \mu\text{J}$  with a pulse repetition frequency of 12 kHz and a pulse duration of 800 ns. With a further amplification stage,  $750\ \mu\text{J}$  pulses were obtained in the laboratory at 5 kHz and  $1\ \mu\text{s}$  with excellent beam quality.

A Doppler heterodyne LIDAR has been developed based on the  $120\ \mu\text{J}$  laser source with a high-isolation free-space circulator. The LIDAR includes a real-time display of the wind field. Wind dispersion is postprocessed.

Field tests were carried out at Orly airport in April 2008. Axial aircraft wake vortex signatures have been successfully observed and acquired at a range of 1.2 km with axial resolution of 75 m for the first time with fiber laser source.

This study was undertaken in the framework of FIDELIO program and is aiming at meeting commercial aircraft requirements for onboard implementation of a wake vortex sensor. Among its results, the project has generated important advances in research and development on fiber laser technology.

## APPENDIX

In this appendix, we will describe the signal processing used with simulated results shown in Fig. 1. The signal processing is based on a maximum-likelihood estimator for simulated accumulated periodogram data.

Assuming that the accumulated periodogram has a  $\chi^2$ -statistic with  $M$  DOF,  $M$  being the number of accumulated periodograms, the likelihood of the signal is given by

$$P(X) = \frac{M^{NM}}{\Gamma^N(M)} \prod_{i=1}^N \frac{X_i^{M-1}}{S_i^M} e^{-M \sum_{i=1}^N X_i/S_i}$$

where  $S$  is a parametric spectrum model and  $N$  is the number of spectral bins of the periodogram. Three parameters are taken into account in the model:

- 1) the CNR;
- 2) the mean velocity  $v_{\text{mean}}$  in the probed volume;
- 3) the wind dispersion  $\sigma_v$  in the probed volume.

The maximum-likelihood estimator finds the parameters (CNR,  $v_{\text{mean}}$ ,  $\sigma_v$ ) that maximize the log-likelihood  $\ln P(X)$  using an optimization algorithm.

Precise details about the computation of the spectrum  $S$ , using the “feuilleté” model, can be found in [4].

## ACKNOWLEDGMENT

The authors would like to thank T. Peschel from Fraunhofer Institute for lending the scanner. They would also like to thank FIDELIO project partners: ELOP (IL, Coordinator, laser integration), Thales R&T (F, laser research), INESC Porto (P, laser research), IPHT (D, fiber research and design), CeramOptec (D, fiber packaging), and Thales Avionics (F, aircraft integration specifications).

## REFERENCES

- [1] S. M. Hannon and J. A. Thomson, "Aircraft wake vortex detection and measurement with pulsed solid-state coherent laser radar," *J. Mod. Opt.*, vol. 41, pp. 2175–2196, 1994.
- [2] S. Rahm, I. Smaliko, and F. Kopp, "Characterization of aircraft wake vortices by airborne coherent Doppler lidar," *J. Aircraft*, vol. 44, no. 3, pp. 799–805, 2007.
- [3] K. Asaka, S. Kameyama, T. Ando, Y. Hirano, H. Inokuchi, and T. Inagaki, "A 1.5  $\mu\text{m}$  all-fiber pulsed airborne Doppler lidar system," Jpn. Aerosp. Exploration Agency (JAXA) IS17-06, 2003.
- [4] D. Douxchamps, Y. Verschuere, S. Lugan, L. Mutuel, B. Macq, and K. Chihara, "On-board axial detection of wake vortices using a 2  $\mu\text{m}$  LiDAR," *IEEE Trans. Aerosp. Electron. Syst.*, vol. 44, no. 4, pp. 1276–1290, Oct. 2008.
- [5] P. Salamitou, A. Dabas, and P. H. Flamant, "Simulation in the time domain for heterodyne coherent laser radar," *Appl. Opt.*, vol. 34, no. 3, pp. 499–506, 1995.
- [6] M. Valla, "Etude d'un Lidar Doppler Impulsionnel à Laser Erbium Fibré pour des Mesures de Champ de Vent dans la Couche Limite de l'Atmosphère," Ph.D. dissertation, Ecole Nationale Supérieure des Télécommunications (ENST), Paris France, 2005.
- [7] C. Brooks and D. Di Teodoro, "Multimewatt peak-power, single-transverse-mode operation of a 100  $\mu\text{m}$  core diameter, Yb-doped rodlike photonic crystal fibre amplifier," *Appl. Phys. Lett.*, vol. 89, pp. 111119-1–111119-3, 2006.
- [8] G. Kulcsar, Y. Jaouën, G. Canat, E. Olmedo, and G. Debarge, "Multiple-stokes stimulated Brillouin scattering generation in pulsed high-power double-cladding  $\text{Er}^{3+}$ - $\text{Yb}^{3+}$  codoped fiber amplifier," *IEEE Photon. Technol. Lett.*, vol. 15, no. 6, pp. 801–803, Jun. 2003.
- [9] H. L. Offerhaus, N. G. Broderick, D. J. Richardson, R. Sammut, J. Caplen, and L. Dong, "High-energy single-transverse mode Q-switched fibre laser based on a multimode large-mode-area erbium-doped fibre," *Opt. Lett.*, vol. 23, pp. 1683–1685, 1998.
- [10] A. Carter, J. Farroni, K. Tankala, B. Samson, D. Machewirth, N. Jacobson, W. Torruellas, Y. Chen, M. Cheng, A. Galvanauskas, A. Sanchez, "Robustly single-mode polarization maintaining Er/Yb co-doped LMA fiber for high power applications," in *Proc. Conf. Lasers Electro-Opt./Quantum Electron. Laser Sci. Conf. Photon. Appl. Syst. Technol.* (OSA Technical Digest Series) Washington, DC: Opt. Soc. Amer., 2007, 1–2, Paper CTuS6 (on CD).
- [11] V. Philippov, C. Codemard, Y. Jeong, C. Alegria, J.-K. Sahu, and G. N. Pearson, "High-energy in-fibre pulse amplification for coherent lidar applications," *Opt. Lett.*, vol. 29, no. 22, pp. 2590–2592, 2004.
- [12] V. Philippov, J. K. Sahu, C. Codemard, W. A. Clarkson, J.-N. Jang, J. Nilsson, and G. N. Pearson, "All-fibre 1.15 mJ pulsed eye-safe optical source," *Proc. SPIE*, vol. 5335, pp. 1–7, 2004.
- [13] G. Canat, L. Lombard, S. Jetschke, S. Unger, J. Kirchoff, H.-R. Müller, A. Durécu, V. Jolivet, and P. Bourdon, "Er-Yb-doped LMA fibre structures for high energy amplification of narrow linewidth pulses at 1.5  $\mu\text{m}$ ," in *Proc. Conf. Lasers Electro-Opt./Quantum Electron. Laser Sci. Conf. Photon. Appl. Syst. Technol.* (OSA Technical Digest Series). Washington, DC: Opt. Soc. Amer., 2007, pp. 1–2, Paper CTuBB1 (on CD).
- [14] C. E. Dilley, M. A. Stephen, and M. P. Savage-Leuchs, "High SBS-threshold, narrowband, erbium codoped with ytterbium fiber amplifier pulses frequency doubled to 770 nm," *Opt. Exp.*, vol. 15, pp. 14389–14395, 2007.
- [15] G. Canat, S. Jetschke, S. Unger, L. Lombard, P. Bourdon, J. Kirchoff, V. Jolivet, A. Dolfi, and O. Vasseur, "Multifilament-core fibers for high energy pulse amplification at 1.5  $\mu\text{m}$  with excellent beam quality," *Opt. Lett.*, vol. 22, no. 33, pp. 2701–2703, 2008.
- [16] S. Wielandy, "Implications of higher-order mode content in large mode area fibers with good beam quality," *Opt. Exp.*, vol. 15, pp. 15402–15409, 2007.

**Agnès Dolfi-Bouteyre** received the M.S. degree from the Ecole Supérieure d'Optique, Orsay, France, in 1986, and the Ph.D. degree in physics from the University Paris XI Orsay, in 1990.

In 1990, she joined the French Aeronautics and Space Research Center (ONERA), Palaiseau, France, where she has been involved in light detection and ranging (LIDAR) systems development for defense or aerospace.

**Guillaume Canat** received the M.S. degree from the Ecole Polytechnique, Palaiseau, France, in 2000, and the Ph.D. degree from the Ecole Nationale Supérieure de l'Aéronautique et de l'Espace, Toulouse, France, in 2006.

Since 2002, he has been a Research Scientist at the French Aeronautics and Space Research Center (ONERA), Palaiseau. His current research interests include high-power fiber laser sources, nonlinear effects in fibers, and coherent combining.

**Mathieu Valla** was born in France in 1976. He received the Engineering and Ph.D. degrees from Telecom Paristech, Paris, France, in 2001 and 2005, respectively.

Since 2002, he has been a Research Engineer at the French Aeronautics and Space Research Center (ONERA), Palaiseau, France.

**Béatrice Augère** was born in 1961. She received the Ph.D. degree in nonlinear optics from the University Paris XI Orsay, France, in 1988.

Since 1989, she has been with the French Aeronautics and Space Research Center (ONERA), Palaiseau, France, where she is currently a Research Scientist in the Lasers and Optoelectronics Research Unit. Her current research interests include light detection and ranging (LIDAR), laser propagation in turbulent, and coherent detection.

**Claudine Besson** received the Ph.D. degree in physics from the Optics Graduate School, Paris, France, in 1989.

She is currently a Senior Scientist and the School Learning Solutions (SLS) Group Leader at the French Aeronautics and Space Research Center (ONERA), Palaiseau. Her current research interests include fiber lasers and light detection and ranging (LIDAR).

**Didier Goular** was born in 1962. He received the Electr. Eng. degree from the Conservatoire national des arts et métiers (CNAM), Paris, France, in 1990.

Since 1985, he has been with the French Aeronautics and Space Research Center (ONERA), Palaiseau, France, where he is currently with the Lidar Team, and is engaged in optimization of electronic and informatics processing of the coherent optical system.

**Laurent Lombard** received the M.S. degree from the Ecole Supérieure d'Optique, Orsay, France, in 2001, and the Ph.D. degree in optics from the University of Paris XI, Orsay, in 2005.

Since 2006, he has been a Research Scientist in the Département Optique Théorique et Appliquée, French Aeronautics and Space Research Center (ONERA), the French Aerospace Laboratory, Palaiseau, France. His current research interests include high-power fiber laser sources, nonlinear effects in fibers, optical beam processing, light detection and ranging (LIDAR), and coherent combining.

**Jean-Pierre Cariou** was born in 1958. He received the Engineering degree in optics from the Ecole Supérieure d'Optique, Orsay, France, and the Ph.D. degree in astronomy and spatial techniques from the University Paris 7 Jussieu, Paris, France, in 1983.

For ten years, he was the Head of the Laser and Optoelectronics Research Group, French Aeronautics and Space Research Center (ONERA), where he later became a Special Adviser for laser applications in the Optics Department (DOTA), and was involved in coherent light detection and ranging (LIDAR) and laser imagers. In 2007, he joined Leosphere Company, Orsay, as a Technical Director for developing commercial wind and aerosol LIDARs for atmospheric applications.

**Anne Durecu** received the M.S. degree from the Institut National des Télécommunications (INT), Evry, France, in 2001, and the Ph.D. degree in physics from the University of Limoges, Limoges, France, in 2005.

Since 2006, she has been a Research Scientist at the French Aeronautics and Space Research Center (ONERA), Palaiseau, France. Her current research interests include high-power fiber lasers.

**Didier Fleury** was born in 1954. He received the Engineering degree in physics and metrology from the Conservatoire national des arts et métiers (CNAM), Paris, France.

He is currently with the Laser Sources and Coherent Lidar Systems (SLS) Unit, French Aeronautics and Space Research Center (ONERA), Palaiseau, France.

**Laurent Bricteux** received the Degree in mechanical engineering and the Ph.D. degree from the Université catholique de Louvain, Louvain-la-Neuve, Belgium, in 2000 and 2008, respectively.

From 2000, he worked for three years as an Engineer at LMS international, Leuven, Belgium, in the field of numerical simulation of vibroacoustic and aeroacoustic phenomena. In 2004, he joined the Research Group in Turbulence and Vortical flows of Prof. G. Winckelmans. He also participated to several research projects related to aircraft wake vortices funded by the European Union. He is currently working on research contracts in aeronautics and energetics

**Sébastien Brousmiche** (M'06) was born in Tournai, Belgium, in 1980. He received the Electr. Eng. degree from the Ecole Centrale des Arts et métiers (CNAM), Bruxelles, Belgium, in 2002, and the D.E.A. degree in electrical engineering from the Université Catholique de Louvain (UCL), Louvain-la-Neuve, Belgium, in 2005, where he is currently working toward the Ph.D. degree.

Since 2004, he has been a Research Engineer with the Communication and Remote Sensing Laboratory, UCL.

**Sébastien Lugan** received the Master's degree from the École Supérieure d'Ingénieurs en Électronique et Électrotechnique (ESIEE), Paris, France, in 2003, and the D.E.A. degree from Gaspard-Monge Institute of Electronics and Computer Science, Université de Marne-La-Vallée, France. He is currently working toward the Ph.D. degree at the Communications and Remote Sensing Laboratory, Université catholique de Louvain, Louvain-la-Neuve, Belgium.

His current research interests include medical imaging, mega-image navigation, and light detection and ranging (LIDAR) detection of wake vortices.

**Benoit Macq** (F'xx) was born in 1961. He received the Electrical engineering and the Ph.D. degrees from the Université catholique de Louvain (UCL), Louvain-la-Neuve, Belgium, in 1984 and 1989, respectively.

He is currently a Professor at UCL in the Communication and Remote Sensing Laboratory.

Dr. Macq has been Guest Editor for the Proceedings of the IEEE and for the *Signal Processing Journal* and member of the program committee of several IEEE and SPIE conferences. He received the Bell Telephone award in 1990.